ELSEVIER

Journal of Power Sources 110 (2002) 295–309

JOURNAL OF POWER SOURCES

www.elsevier.com/locate/jpowsour

# Mathematical modeling of high-power-density insertion electrodes for lithium ion batteries

Mark W. Verbrugge[a,*], Daniel R. Baker[b], Brian J. Koch[c]

[a]General Motors Research and Development Center, Warren, MI 48090-9055, USA
[b]General Motors Fuel Cell Propulsion Center, Warren, MI 48090-9055, USA
[c]General Motors Advanced Technology Vehicles, 1996 Technology Drive, Troy, MI 48007-7083, USA

**Abstract**

Theoretical calculations are compared with well-controlled experiments conducted on a high-surface area, small diameter lithiated-carbon electrodes. The electrodes are shown to yield very high current densities and exhibit little interfacial kinetics resistance or intercalate diffusion resistance. The mathematical treatment describes quantitatively a wide range of electrochemical experiments. The application of the model to the experimental data is facilitated by the use of a reference electrode. Initial cycling behavior of the high-surface-area electrode is elucidated, including clarification of the first-cycle coulombic inefficiency. Nitrogen absorbtion and scanning electron micrographs are utilized to ascertain the microstructural characteristics that distinguish the active electrode material. An asymptotic analysis is used to indicate when diffusion resistance within host particles is negligible; this fact simplifies model calculations and contributes to our overall understanding of insertion processes associated with host particles of very small dimensions.


*Keywords:* Battery modeling; High-power batteries; Lithium carbon; Vapor-grown carbon fibers

## 1. Introduction

Although the safety and performance benefits associated with using lithiated carbon over metallic lithium in room-temperature, solvent-based lithium batteries are well accepted, elucidating the processes governing the performance of the lithiated-carbon electrode remains a challenging research objective [1–9,19]. It is the purpose of this work to contribute to the research and development of lithiated carbon anodes by extending previous characterization methods and tools to examine a high-power carbon anode material, which may be of interest for electric and hybrid vehicle applications.

The vapor-grown carbon fibers used in this study are described in [10–12]. We examine electrodes made from these fibers and highlight the material's high-power capability derived from the small diameter of the carbon fibers. Scanning electron micrographs, nitrogen adsorption data, and electrochemical experiments are reported, all of which are employed in the modeling analysis.

The mathematical description we employ to simulate the cyclic voltammetry experiments is analogous to that developed for the modeling of batteries containing porous insertion electrodes, with the primary exception being the treatment of transport within the solid state [1,4,5,7,9,19]. References to early work concerned with the treatment of insertion electrodes can be found in the paper by West et al. [13], which provides a treatment of porous electrodes constructed with insertion materials, and related theoretical investigations of metal-hydride electrodes [14–16]. Verbrugge and Koch [3,4] purpose and implement a procedure to analyze lithium intercalation of single-fiber electrodes, allowing one to isolate the properties intrinsic to the lithiated carbon fiber; the results are not complicated by the influence of binders, electronically conductive additives, current collectors, or other components necessary for the fabrication of porous carbon electrodes such as those used in this investigation. For the current investigation, however, the fibers are of extremely small diameter, and in Appendix B, it is shown that diffusion within the carbon fibers of the electrode takes place fast enough so that transport is in quasi-steady state. This fact simplifies greatly the model calculations and facilitates our understanding of what processes govern the electrode behavior. In general, the asymptotic analysis given in Appendix B can also be applied to other insertion-electrode materials in order to determine if diffusion resistance of the guest species within the solid state needs to be considered. We apply the model to examine the porous lithiated-carbon electrode in an electrochemical cell of

* Corresponding author.
*E-mail address:* mark.w.verbrugge@gm.com (M.W. Verbrugge).

0378-7753/02/$ – see front matter 
PII: S0378-7753(02)00192-1

known dimensions and containing a reference electrode [17,18] as well as a counter electrode.

## 2. Experimental

### 2.1. Materials

Solutions were made with distilled propylene carbonate and reagent-grade, dried lithium perchlorate (Aldrich). For all of the data discussed in this study, a 1 M $LiClO_4$+ propylene carbonate electrolyte was employed, and the temperature was maintained at 25 °C. A description of the purification procedures used is given in [3]. Lithium (Foote Mineral, 99.99%) was used to construct the counter electrode. Aluminum wire (Johnson Matthey, 100 μm diameter, 99.999%) was alloyed with lithium at a current density of 10 μA/cm$^2$ until the average composition reached 2 mole percent. The current was passed between the aluminum wire and the lithium foil that later became the counter electrode. The lithium aluminum reference maintained a stable open-circuit potential, 0.387 V versus the lithium foil, throughout the experiment duration, in agreement with previous investigations [20]. All experiments were conducted in a vacuum atmospheres glove box fed with 99.999% argon gas (Scott speciality gases). Provisions were made to remove trace amounts of oxygen and water.

### 2.2. Electrochemical cell

A schematic illustration of the three-electrode cell is shown in Fig. 1. The porous carbon electrode is located 1 mm away from the lithium–aluminum reference wire and 2 mm away from the lithium counter electrode. The superficial area of the working and counter electrodes was 3.88 cm$^2$. The cells were controlled by an EG & G Princeton Applied Research Potentiostat/Galvanostat Model 273, and the data was collected with a Nicolet 4094B Storage Oscilloscope connected to a laboratory computer. For all of the data presented, a negative current denotes an overall cathodic process.

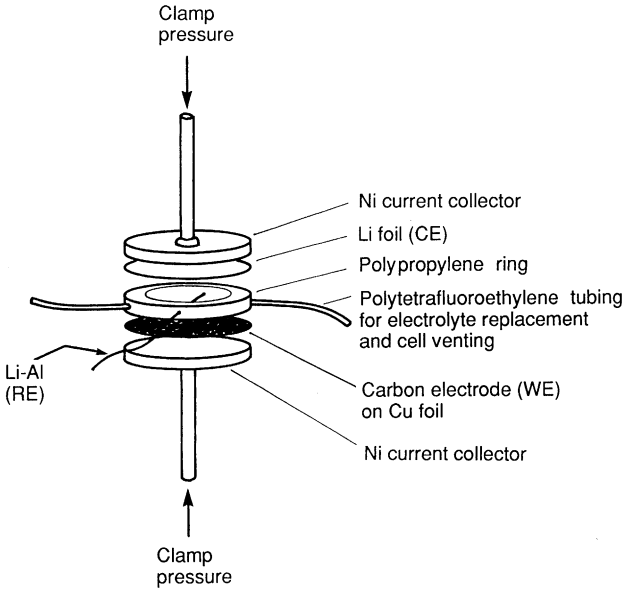


Fig. 1. Electrochemical cell. The porous carbon electrode is located 1 mm away from the 100-μm diameter lithium–aluminum (reference) wire and 2 mm away from the lithium counter electrode. The superficial area of the working and counter electrodes was 3.88 cm$^2$.

### 2.3. Porous carbon electrodes

The carbon electrodes of this study were made from a vapor-grown carbon fiber that has been described by Tibbetts

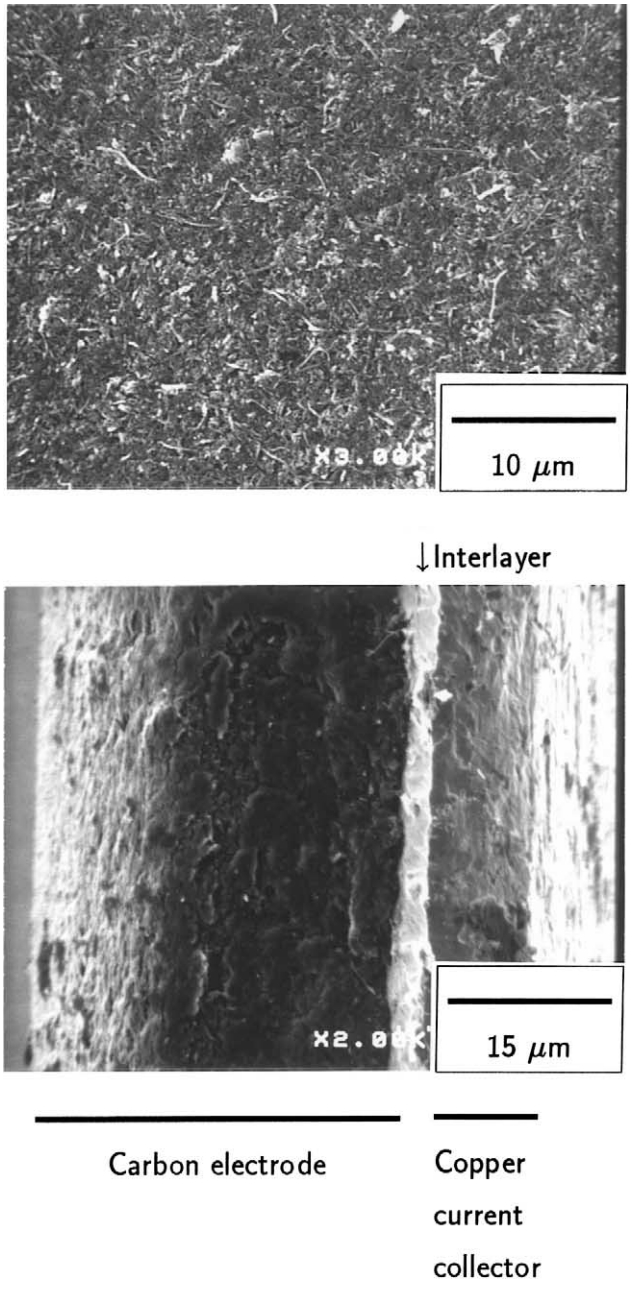


Fig. 2. Upper micrograph: electrode surface; lower micrograph: electrode cross-section.

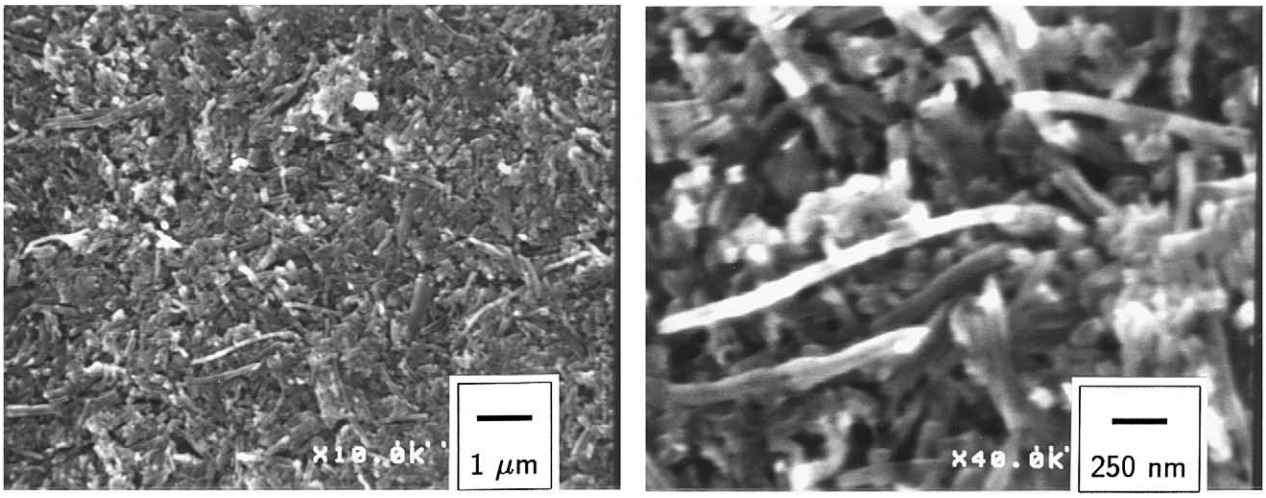


Fig. 3. High-magnification electrode micrographs.

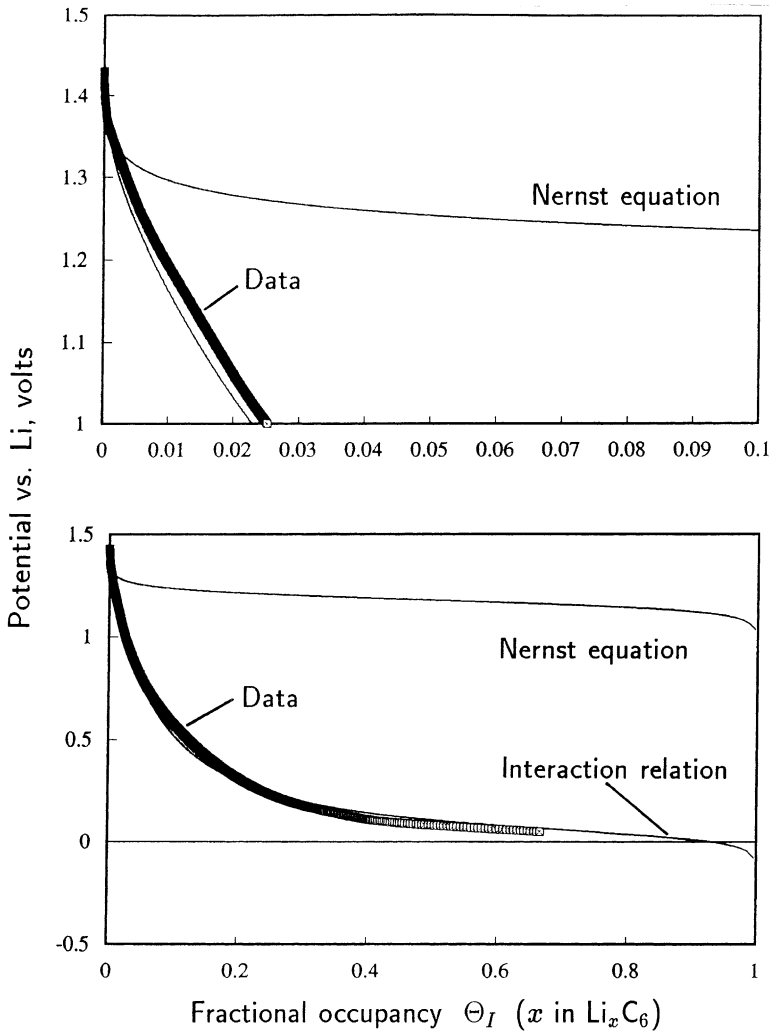


Fig. 4. Pseudo-thermodynamic data. The experimental data are shown to be well represented by Eq. (A.3), corresponding to the curve labeled Interaction relation. The top panel shows that the Interaction model is in good agreement with the cell Nernst equation (Eq. (A.2) with $V_{I-I} = 0$) for dilute lithium ($\Theta_I \gg 1$).

et al. [10,12,13]. The density of the fibers is $2.02 \pm 0.02$ g/cm$^3$, which can be compared with 2.26 g/cm$^3$ for graphite [12]. The fibers were grown by Applied Sciences. The electrode porosity after compression at 650 psi and 80 °C was 20%.

Low-magnification electron micrographs of the face and cross-section of the electrodes are shown in the upper and lower pictures of Fig. 2, respectively. The thickness of the porous electrode was 35 μm. Higher magnification images of the electrode face are displayed in Fig. 3, wherein the fibrous nature of the active material is immediately apparent. By measuring the resistance between the electrode face and current collector, we determined an effective solid-phase conductivity of $3.2 \times 10^{-4}$ S/cm. Neither the effective solid-phase conductivity nor the electrode thickness changed substantially after soaking the electrode in the electrolyte for 24 h.

Nitrogen adsorption measurements (using a Quantachrome Autosorb-1 automated gas adsorption system) yielded a surface area of 3 m$^2$/g for the solvent-cast electrode, corresponding to a specific surface of about 60,000 cm$^2$/cm$^3$. As will be shown in Section 4, a specific surface of 2000 cm$^2$/cm$^3$ was used to represent the experimental data, perhaps indicating that not all of the surface carbon is active for electrochemical reaction. The surface-area measurements on actual electrodes, however, reflect the influence of binder materials and current collector and in general are quite approximate. Fong et al. [22] have shown that the initial capacity loss scales with surface area for petroleum cokes, but no surface-area dependence was observed for graphites.

## 3. Mathematical model

We have placed all of the mathematical development in Appendixes A and B. The approach taken in treating the thermodynamics and electrochemical kinetics derives from the characterization of partially graphitized single-fiber microelectrodes [4]. The description of the transport phenomena for the liquid phase and the treatment of ohmic loses in the solid phases corresponds closely to those derived and implemented in [1]. The inclusion of the Appendix is motivated by two considerations: (1) it is unlikely that the simulations presented in this paper could be understood or reproduced by future researchers without a complete listing of the equations solved (Appendix A) and (2) an asymptotic analysis is used to show that when diffusion resistance within the carbon fibers of the electrode is negligible, the governing equations for the lithium ion cell can be greatly simplified (Appendix B). The resulting mathematical model comprises a set of coupled, multivariable, nonlinear differential equations, which were solved using the routine described in [21].

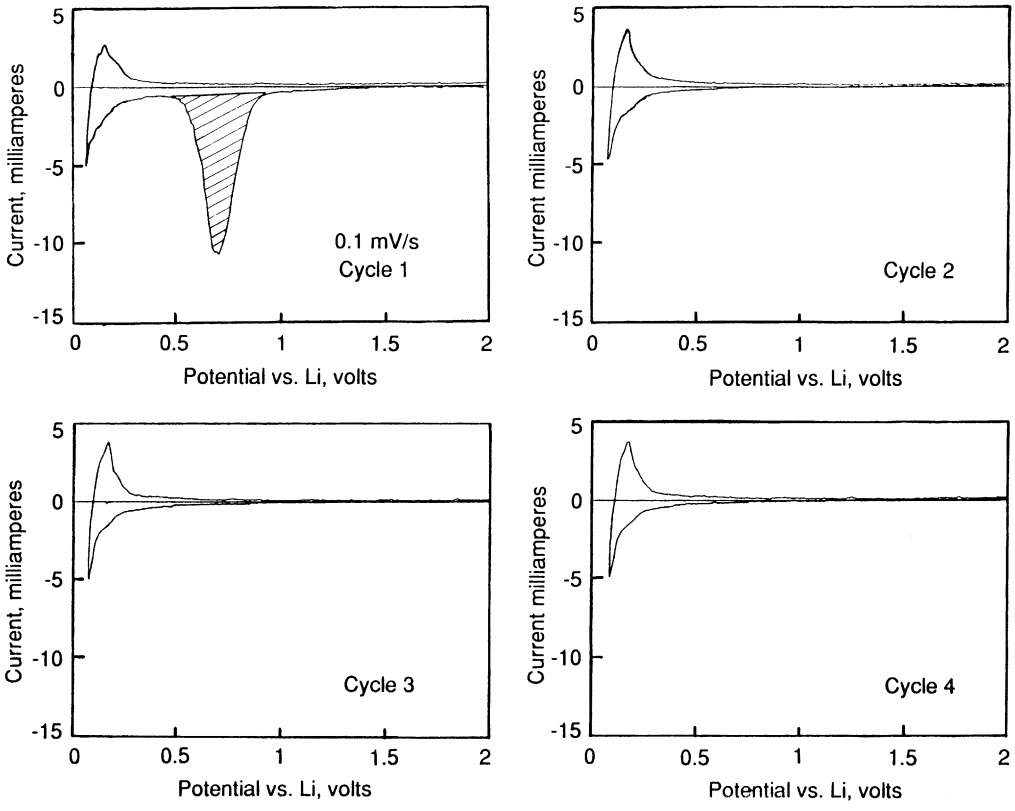


Fig. 5. First-cycle inefficiency. The shaded cathodic peak centered at 0.7 V corresponds to solvent reduction. The uniform and sustained periodic state is obtained after the fourth cycle.

## 4. Results and discussion

### 4.1. First-cycle inefficiency and electrode conditioning

An aspect of the performance of lithiated carbon electrodes that is still not fully understood concerns the loss of capacity on the first cycle of the electrode [22,33–36]. As is shown clearly in the top, left panel of Fig. 5, a large peak in the current response is seen on the first cycle when the carbon electrode is (cathodically) charged, and the corresponding first (anodic) discharge yields a cycle efficiency of 26 precent during the subsequent anodic portion of the cycle. It can be postulated that the large cathodic peak current starting at about 0.8 V corresponds to the reduction of propylene carbonate to form propylene gas and carbonate anion by an overall process involving two electrons [37,38]. The evolution of gas from the cell, vented through the tubing shown in Fig. 1, supports this speculation. Upon subsequent cycles, however, no further evidence of solvent reduction or cycle inefficiency is observed, as indicated by the voltammograms for cycles 2–4 of Fig. 5. Thus, it appears that the carbon sites active in the solvent reduction process are de-activated during the first intercalation half cycle. Note that the lithium de-intercalation current observed during the first de-intercalation half cycle yields less anodic charge than subsequent de-intercalation half cycles, reflecting that the cathodic charge associated with gas evolution cannot be recovered anodically.

From a practical perspective, one needs only to cycle the electrode once to remove the solvent reduction process. Since it is common to fabricate cells with discharged carbon electrodes (devoid of lithium) and discharged metal oxide cathodes (containing lithium), one can simply cycle the electrode once at 0.1 mV/s, terminate the procedure upon completion of the cycle at 2 V versus Li, and use subsequently the wetted electrode in a battery with the expectation of

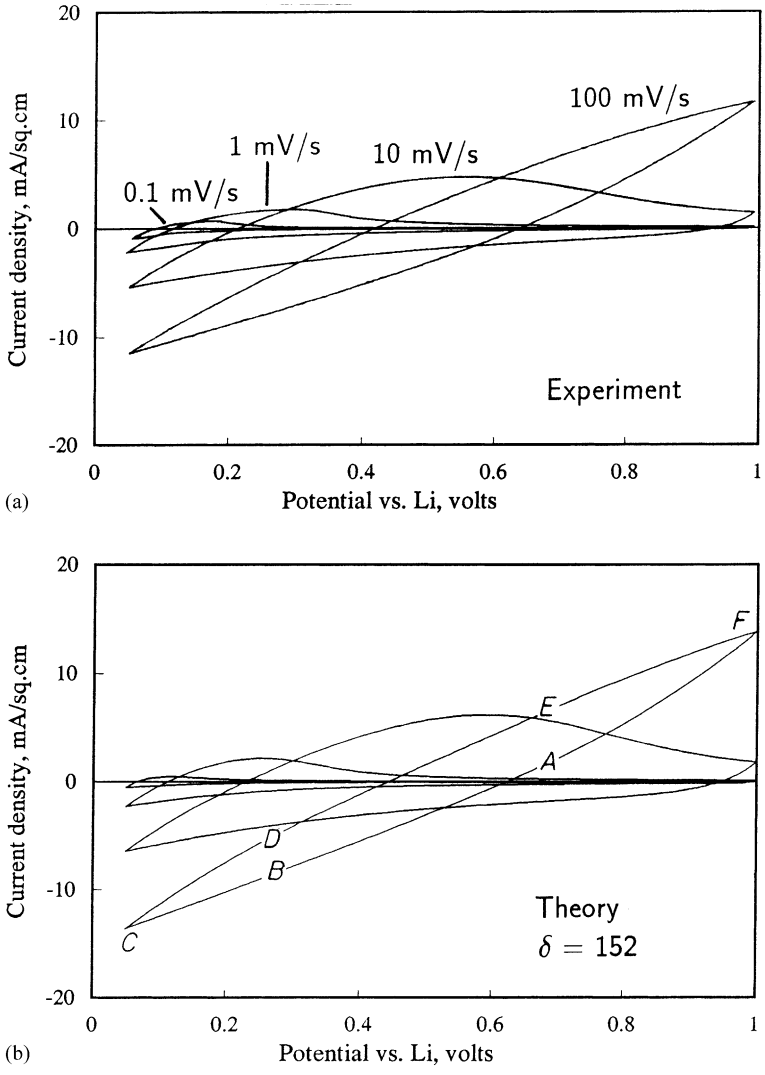


Fig. 6. Experiment–theory comparison. Both the experimental (upper figure) and theoretical (lower figure) results correspond to the uniform and sustained periodic state. The potential scan rate is indicated, and the letters A–F refer to the electrode potential and correspond to the same letters appearing in Figs. 7–10.

Table 1
Parameters and properties

| Quantity | Value | Units |
|---|---|---|
| $a_s$ | 2000 | $cm^2/cm^3$ |
| $c^0$ | 1.3 | M |
| $c_{ref}$ | 1 | M |
| $c_s$ | 5.1 | M |
| $D$ [28] | $4.2 \times 10^{-6}$ | $cm^2/s$ |
| $i_{0,ref}$ [4] | 1 | $mA/cm^2$ |
| $\ell_1$ | 2 | mm |
| $\ell_2$ | 35 | μm |
| $t_+^0$ [1,39] | 0.2 | – |
| $T$ | 298 | K |
| $\beta$ [4,28] | 0.5 | – |
| $\epsilon_1$ | 0.8 | – |
| $\epsilon_2$ | 0.2 | – |
| $\epsilon_e$ | 1 | – |
| $\sigma$ | $3.2 \times 10^{-4}$ | S/cm |
| $\nu$ | 2 | – |

These values yield $\delta = 152$; $\delta$ is the lone dimensionless parameter that is adjusted to fit the data shown in Fig. 6.

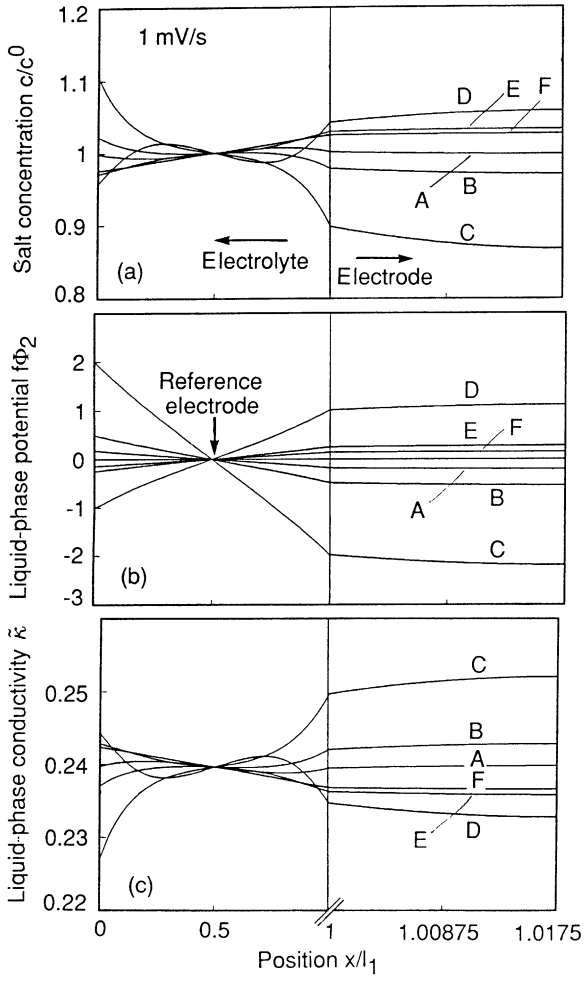


Fig. 7. Profiles of the dimensionless salt concentration $C = c/c^0$ (a), liquid-phase potential $\Psi_2 = f\Phi_2$ (b), and liquid-phase conductivity $\tilde{\kappa}(C) = F^2\kappa(c)/(Fc^0D)$ (c). The letters A–F refer to the potentials indicated by the corresponding letters in Fig. 6 (potential scan rate: 1 mV/s).

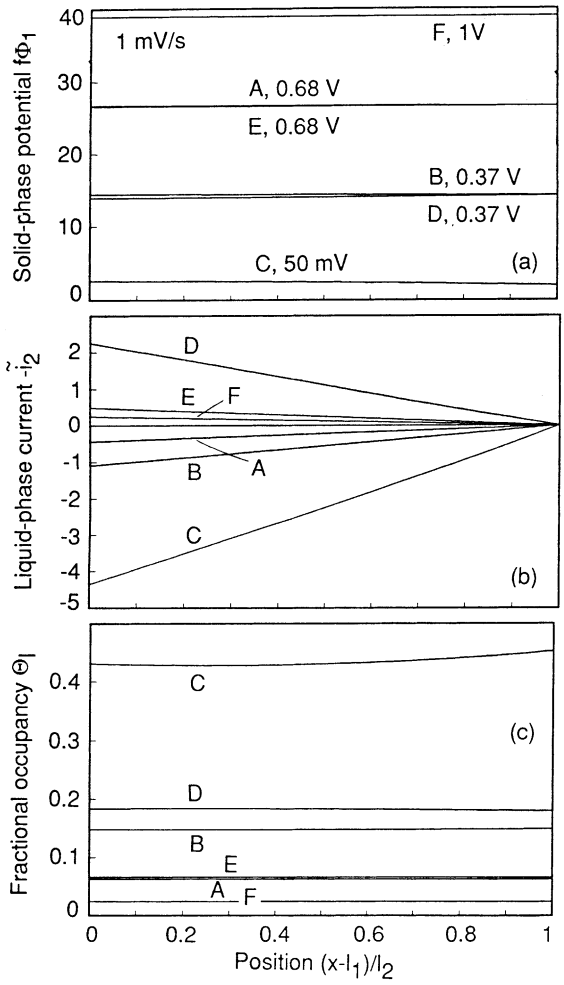


Fig. 8. Profiles of the dimensionless solid-phase potential $\Psi_1 = f\Phi_1$, current density in the liquid phase $\tilde{i}_2 = \ell_1 i_2/(Fc^0D)$, and fractional occupancy in the intercalation host carbon $\Theta_1$ (potential scan rate: 1 mV/s).

nominally 100 percent for ensuing cycles. Provision must be made for loss of lithium, however.

### 4.2. Experiment–theory comparison

The upper curves in Fig. 6 correspond to the uniform and sustained periodic state and potential scan rates of 0.1, 1, 10, and 100 mV/s. Calculations from the theoretical model are displayed in the lower panel. Both experimentally and theoretically, the uniform and sustained periodic state is obtained after about two cycles for the slow potential scan rates and after about four cycles for the 10 and 100 mV/s scan rates. The calculations are for the fourth cycle—calculations for subsequent cycles plot over the curves and are not discernible from those displayed.

The parameters and properties employed in the simulations are given in Table 1. In particular, we note that $\delta$ is the only unknown dimensionless parameter. The exchange current density and symmetry factor were taken to be those measured in [4] on individual carbon fibers. A symmetry

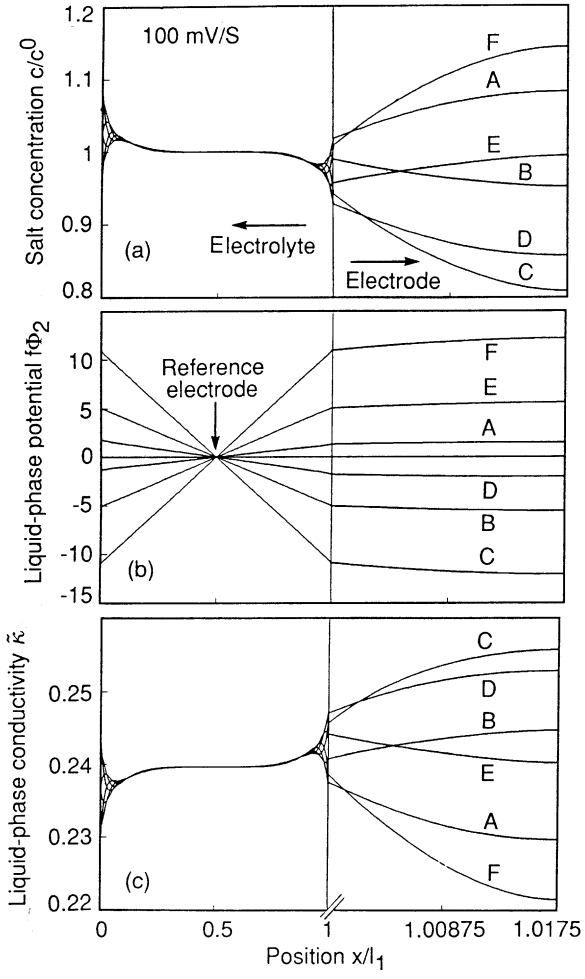


Fig. 9. Profiles of the dimensionless salt concentration $C$ (a), liquid-phase potential $\Psi_2$ (b), and liquid-phase conductivity $\tilde{\kappa}(C)$ (c). The letters A–F refer to the potentials indicated by the corresponding letters in Fig. 6 (potential scan rate: 100 mV/s).

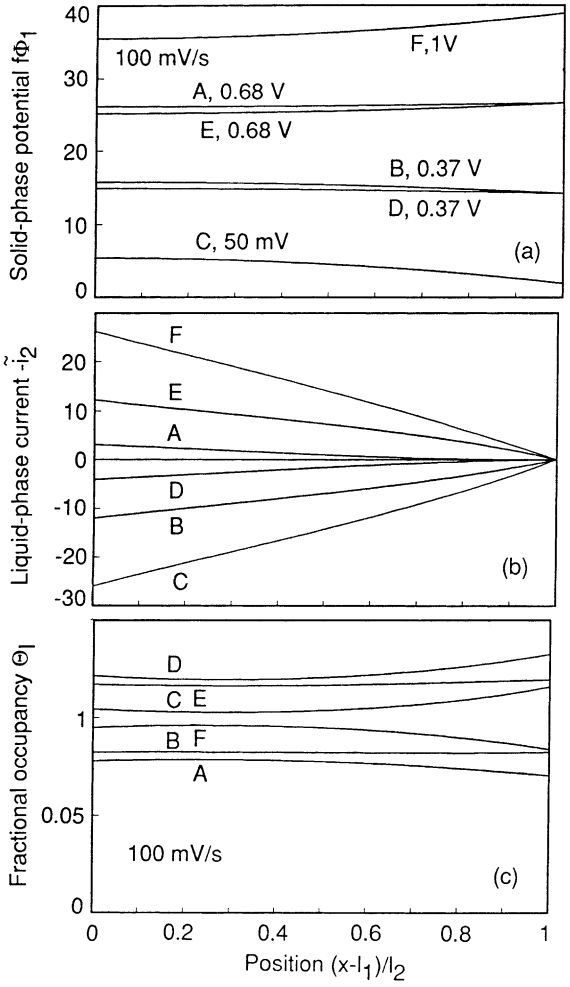


Fig. 10. Profiles of the dimensionless solid-phase potential $\Psi_1$, current density in the liquid phase $\tilde{i}_2$, and fractional occupancy in the intercalation host carbon $\Theta_I$ (potential scan rate: 100 mV/s).

factor of 0.5 was also measured for the Li–$Li^+$ reaction in [28], wherein the quantity $D/(1-t_0^+)$ was found to be constant for salt concentrations below 1 M. The specific surface area $a_s$ (and thus $\delta$) was fitted to the data. The sensitivity of the simulated voltammograms to this parameter is discussed below.

Although the curves display a wide variation in structure, both along an individual curve and from curve to curve, the mathematical description is shown to capture the apparent features of the experimental data. Differences between any two electrodes are of the magnitude of the differences between the experimental data and theoretical calculations, and it would be unproductive to adjust further the various model parameters in order to improve the experiment–theory agreement.

### 4.3. Concentration, potential, and conductivity profiles

Profiles of the dimensionless salt concentration $C$, liquid-phase potential $\Psi_2$, liquid-phase conductivity $\tilde{\kappa}$, solid-phase potential $\Psi_1$, current density in the liquid phase $\tilde{i}_2$, and fractional occupancy within the intercalation host carbon $\Theta_I$ are given in Figs. 7 and 8 for a scan rate of 1 mV/s and in Figs. 9 and 10 for a scan rate of 100 mV/s. These dimensionless quantities are defined in Table 3[1] of Appendix A. The profiles correspond to the uniform and sustained periodic state. The electrode potentials are indicated by the symbols A–E (cf. lower panel of Fig. 6). These same electrode potentials correspond to the value of $f\Phi_1$ at $x = \ell_1 + \ell_2$ in the top panels of Figs. 8 and 10. In contrasting the results for 1 and 100 mV/s, we note that the larger potential scan rates yield larger current densities, as the salt concentration is less depleted at the electrode–electrolyte interface during the cycle, the mass-transport resistance is thereby reduced, and the potential drops in both the liquid and solid phases are increased commensurate with the increased current flow. Just as there is less salt reacted

[1] See Table 3 for definitions of dimensionless quantities employed in Table 2.

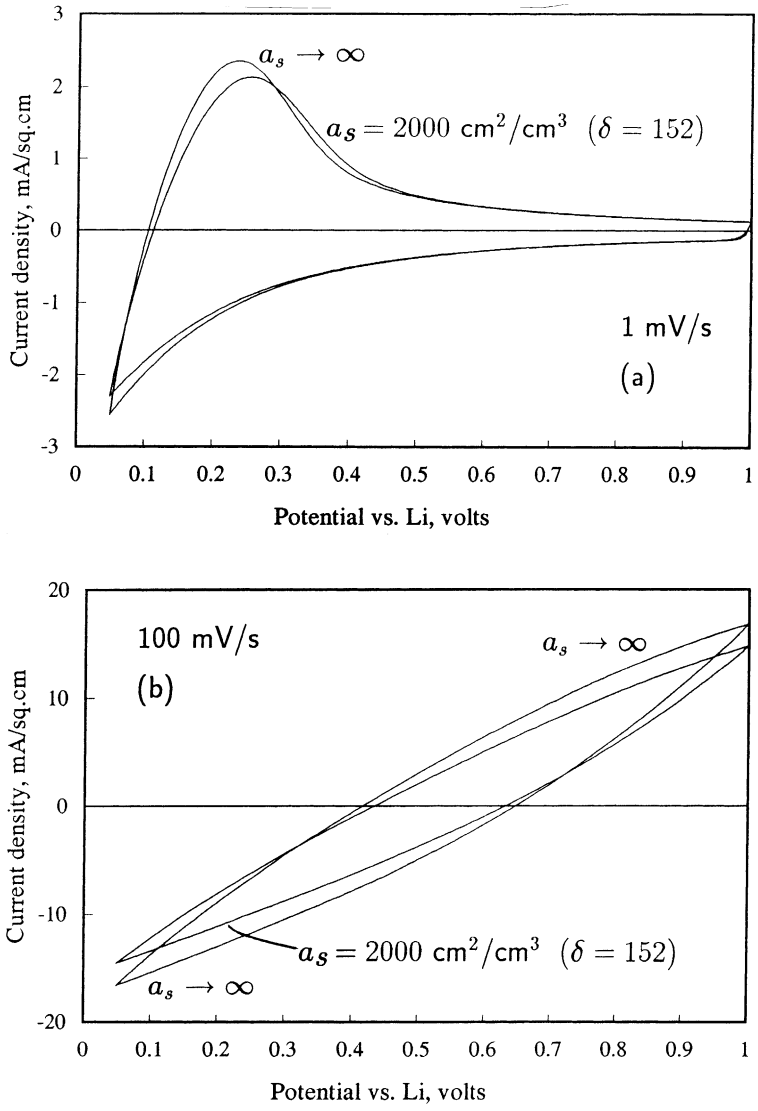


Fig. 11. Sensitivity to the specific surface area $a_s$, which enters the dimensionless formulation through the group $\delta = a_s \ell_1^2 i_{0,\mathrm{ref}}/(c^0 DF)$. For the theoretical calculations shown in Fig. 6, $a_s = 2000\ \mathrm{cm}^2$ (and $\delta = 152$). Upper figure, 1 mV/s; lower figure, 100 mV/s.

per cycle with increasing potential scan rates, the utilization of active material is also diminished, evidenced by the comparison of the $\Theta_I - X$ plots of Figs. 8 and 10.

### 4.4. Sensitivity analyses

An important aspect to understanding the behavior of porous carbon intercalation electrodes is the identification of performance-limiting processes. Although the only parameter adjusted to obtain the theoretical voltammograms shown in Fig. 6 was the specific surface $a_s$, incorporated into the dimensionless group $\delta = a_s \ell_1^2 i_{0,\mathrm{ref}}/(c^0 DF)$, the theoretical results for the uniform and sustained periodic state displayed in Fig. 11 indicate that the calculations of Fig. 6 follow closely those of a kinetically facile electrode reaction ($\delta \rightarrow \infty$), underscoring the facile nature of the Li–$Li^+$ reaction [28] and the utility of employing high-surface-area carbons as lithium-intercalation electrodes. (Note that for the case of $\delta \rightarrow \infty$ there are no adjustable parameters used in the model calculations).

For the conditions and quantity values associated with Fig. 6, the calculations are far less sensitive to the salt diffusion coefficient $D$, lithium-ion transference number $t_+^0$, and solid-phase conductivity $\sigma$ than to the liquid-phase conductivity $\kappa$. The influence of the liquid-phase conductivity on the theoretical voltammograms is illustrated in Fig. 12 for the uniform and sustained periodic state. The solution-phase ohmic drop is influenced additionally by the system geometry (e.g. $\ell_1$ and to a lesser extent $\ell_2$).

## 5. Summary and conclusion

The deliverable energy and power from the lithiated-carbon electrode influence directly the range and acceleration capabilities of electric vehicles utilizing battery systems

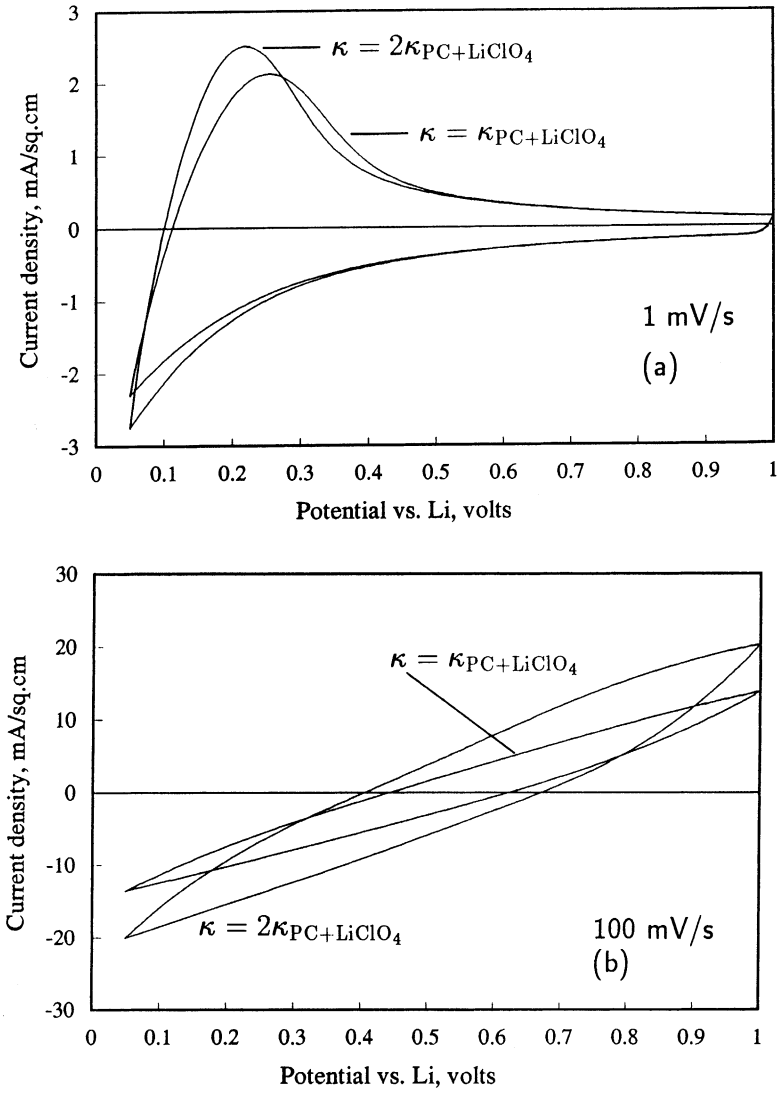


Fig. 12. Sensitivity to the liquid-phase conductivity $\kappa(c)$. The theoretical calculations shown in Fig. 6 utilize $\kappa = \kappa_{PC+LiClO_4}$ [29,30]. Upper figure, 1 mV/s; lower figure, 100 mV/s.

comprising lithiated carbon. For hybrid electric vehicles, the power density plays a critical role, as higher power density batteries allow automakers to reduce the size of the heat engine, thereby improving fuel economy and reducing unwanted emissions. In this work, we compare theoretical calculations—based on the governing thermodynamic, kinetic, and transport phenomena—with well-controlled experiments conducted on high-power lithiated-carbon electrodes that are constructed by a solvent-casting process. The mathematical treatment, which couples the phenomena taking place within insertion electrodes (on a microscopic scale) to macroscopic transport, is shown to describe quantitatively a wide range of electrochemical experiments. In addition, initial cycling of the electrodes is investigated as are microstructural characteristics that distinguish the active electrode materials. The analysis is used to show that the high surface area of the high-power solvent-cast electrode yields little overall electrochemical reaction resistance, and the performance of the cell used in this study is determined primarily by liquid-phase resistance. An asymptotic analysis (Appendix B) is used to show that diffusion resistance within the carbon fibers of the electrode is negligible; this fact simplifies the model calculations and contributes to our overall understanding of insertion processes associated with host particles of very small dimensions. In summary, it is shown quantitatively that the vapor-grown lithiated-carbon electrodes yield very high current densities, consistent with the material requirements of high-power density batteries.

*List of symbols*

| | |
|---|---|
| $a$ | radius of host fibers or particles (cm) |
| $a_s$ | specific surface ($cm^2/cm^3$) |
| $c$ | concentration ($mol/cm^3$) |
| $D$ | diffusion coefficient ($cm^2/s$) |
| $f$ | $F/RT$ ($V^{-1}$) |

| | |
|---|---|
| $f_{\pm}$ | mean molar activity coefficient of the salt |
| $F$ | Faraday's constant (96487 C per equivalent) |
| $\boldsymbol{i}$ | current density (A/cm$^2$) |
| $i_0$ | exchange-current density (A/cm$^2$) |
| $i_{0,\mathrm{ref}}$ | reference exchange-current density (A/cm$^2$) |
| $k_\mathrm{a}$ | anodic rate constant (mol/cm$^2$ s) |
| $k_\mathrm{c}$ | cathodic rate constant (cm/s) |
| $\ell_1$ | thickness of electrolyte region (cm) |
| $\ell_2$ | thickness of porous-electrode region (cm) |
| $n$ | number of electrons per reaction |
| $N$ | flux density (mol/cm$^2$ s) |
| $r$ | radial coordinate (cm) |
| $R$ | gas constant (8.314 J/mol K) |
| $\mathrm{S_C}$ | vacant site within the carbon host |
| $t$ | time (s) |
| $t_i^0$ | transference number of species $i$ (relative to the solvent velocity) |
| $T$ | temperature (K) |
| $U$ | open-circuit potential (V) |
| $\boldsymbol{v}$ | velocity (cm/s) |
| $V_{\mathrm{I-I}}$ | interaction potential contribution (Eq. (A.2)) (V) |
| $x$ | distance coordinate (cm) |
| $z$ | charge number |
| $\alpha$ | dimensionless group $\alpha = ai_{0,\mathrm{ref}}/(FD_\mathrm{I}c_\mathrm{s})$ |
| $\beta$ | transfer coefficient of reaction |
| $\gamma$ | activity coefficient |
| $\epsilon$ | porosity |
| $\zeta$ | dimensionless group $\zeta = (a/\ell_1)^2 D/D_\mathrm{I}$ |
| $\eta_\mathrm{s}$ | surface overpotential (V) |
| $\Theta$ | fractional occupancy |
| $\kappa$ | liquid-phase ionic conductivity (S/cm) |
| $\mu$ | chemical potential (J/mol) |
| $\sigma$ | solid-phase electronic conductivity (S/cm) |
| $\Phi$ | electric potential (V) |

*Superscripts and subscripts*

| | |
|---|---|
| o | pure state |
| $\theta$ | secondary reference state at infinite dilution |
| $+$ | cation ($\mathrm{Li^+}$) |
| $-$ | anion ($\mathrm{ClO_4^-}$) |
| 0 | initial condition or solvent |
| 1 | solid phase |
| 2 | liquid phase |
| e | electrolyte region, $0 < x < \ell_1$ |
| I | guest intercalation species |
| S | vacant host site |
| T | total |

## Appendix A

The thermodynamic and phenomenological equations used in the mathematical model are presented in this section. These equations are then combined with standard conservation equations [17] to derive the governing partial differential equations for the cell model.

### A.1. Thermodynamics

The treatment of both the thermodynamics and interfacial-kinetics of the reaction at the fiber surface follows from the development given in [4], where these phenomena were studied using well-characterized single-fiber electrodes. The electrochemical reaction at the fiber surface is written as

$$\mathrm{Li^+ + e^- + S_C} \underset{k_\mathrm{a}}{\overset{k_\mathrm{c}}{\rightleftharpoons}} [\mathrm{Li}^\chi - \mathrm{S_C}^{-\chi}]. \tag{A.1}$$

A vacant site within the carbon host and available for lithium intercalation is represented by $\mathrm{S_C}$. After insertion, the lithium still retains a significant positive charge $\chi$, and the carbons originally constituting the host site take on a negative charge of equal magnitude, $-\chi$. The open-circuit potential $U$ of the intercalation electrode relative to a metallic lithium electrode, is given by

$$FU = \mu_\mathrm{Li} + \mu_\mathrm{S} - \mu_\mathrm{I},$$

where $F$ refers to the Faraday's constant, $I$ refers to the intercalating species (e.g. $[\mathrm{Li}^\chi - \mathrm{S_C}^{-\chi}]$ of reaction (A.1)), and S refers to a vacant site available for reaction with species $I$ (e.g. $\mathrm{S_C}$ of reaction (A.1)). The chemical potential of the metallic lithium electrode corresponds to that of pure lithium, $\mu^\mathrm{o}_\mathrm{Li}$. To formulate the chemical potentials for the intercalation-electrode species, $\mu_\mathrm{S}$ and $\mu_\mathrm{I}$, a convenient standard state corresponds to an infinitely dilute solution of $I$ in host S. The cell potential is written as

$$U = U^\theta + \frac{RT}{F}\ln\frac{\Theta_\mathrm{S}}{\Theta_\mathrm{I}} + \underbrace{\frac{RT}{F}\ln\frac{\gamma_\mathrm{S}}{\gamma_\mathrm{I}}}_{V_{\mathrm{I-I}}}, \tag{A.2}$$

where $\Theta$ denotes fractional occupancy, $\Theta_\mathrm{I} + \Theta_\mathrm{S} = 1$, $\gamma$ refers to an activity coefficient, [23] and the standard cell potential $U^\theta$, the concentration-independent portion of the cell potential, is given by

$$FU^\theta = \mu^\mathrm{o}_\mathrm{Li} + \mu^\mathrm{o}_\mathrm{S} - \mu^\theta_\mathrm{I}.$$

The reference states require that

$$\gamma_\mathrm{I} \to 1 \quad \text{as} \quad \Theta_\mathrm{I} \to 0 \qquad \gamma_\mathrm{S} \to 1 \quad \text{as} \quad \Theta_\mathrm{S} \to 1.$$

Thus, $\lim_{\Theta_\mathrm{I}\to 0} V_{\mathrm{I-I}} = 0$. Because of the reference states chosen, the deviation from ideal solution behavior is due to $I$-$I$ interactions, resulting in the addition of $V_{\mathrm{I-I}}$ to the Nernst expression for the cell potential. We make the assumption that the contribution of the excess free energy can be expressed as

$$V_{\mathrm{I-I}} = a_1 a_2 \frac{(\Theta_\mathrm{I} + a_3\Theta_\mathrm{I}^2)}{1 + a_1(\Theta_\mathrm{I} + a_3\Theta_\mathrm{I}^2)}, \tag{A.3}$$

where the parameters

$$a_1 = 13, \quad a_2 = 1.13583, \quad \text{and} \quad a_3 = 3$$

were fit to the open-circuit data (cf. Fig. 4). This approach to treating the excess free energy is analogous that originally proposed by Wohl [24] for the treatment of excess functions. We shall refer to Eq. (A.2), with the inclusion of $V_{\text{I–I}}$, as the *interaction relation*. A comparison of the open-circuit potential data with the Nernst equation and the interaction relation is shown in Fig. 4. A value of $U^{\theta} = 1.178$ V was employed. Note that as the fractional occupancy $\Theta_{\text{I}}$ tends to zero, the Nernst equation is recovered for the cell potential, both experimentally and theoretically. The use of the interaction relation allows for the straightforward application of thermodynamic relationships and a convenient algebraic expression for describing the equilibrium behavior.

### A.2. Transport phenomena

Concentrated solution theory [17,25] is used to relate species' fluxes to electrochemical potential gradients:

$$c_i \nabla \mu_i = RT \sum_j \frac{c_i c_j}{c_{\text{T}} D_{ij}} (\boldsymbol{v}_j - \boldsymbol{v}_i). \tag{A.4}$$

The concentration and velocity of species $i$ are given by $c_i$ and $\boldsymbol{v}_i$, respectively. The diffusion coefficient representing the interaction of species $i$ and $j$ corresponds to $D_{ij}$, and $c_{\text{T}}$ represents the total solution concentration including the solvent. For the binary electrolyte of this study, the three diffusion coefficients ($D_{+0}$, $D_{-0}$, and $D_{+-}$) can be replaced with three parameters that are more commonly reported in the literature: the cation transference number (relative to the solvent velocity),

$$t_+^0 = 1 - t_-^0 = \frac{z_+ D_{+0}}{z_+ D_{+0} - z_- D_{-0}},$$

the salt diffusion coefficient,

$$D = \frac{c_{\text{T}}}{c_0} \left(1 + \frac{\mathrm{d} \ln f_{\pm}}{\mathrm{d} \ln c}\right) \frac{D_{+0} D_{-0} (z_+ - z_-)}{z_+ D_{+0} - z_- D_{-0}},$$

and the electrolyte conductivity, which shall be discussed below in the context of the electric potential in solution. Due to lack of experimental data, we shall ignore activity coefficients ($f_{\pm} = 1$) in formulating the electrochemical potentials, making Eq. (A.4) similar to the Stefan–Maxwell relations [26,27]. In addition, the solvent is taken to be immobile and of invariant concentration, and the salt diffusion coefficient and cation transference number are assumed constant. These assumptions should be valid for salt concentrations below 1 M for the system of study [28]. The result is the cation ($\text{Li}^+$) flux relation given as Eq. (A.7). The electric potential in solution $\Phi_2$ is defined in terms of a lithium reference electrode,

$$\text{Li}^+ + \text{e}^- \rightleftharpoons \text{Li}.$$

($\Phi_1$ shall be used to refer to the solid-phase electric potential). At the reference electrode,

$$\mu_{\text{Li}}^+ + \mu_{\text{e}}^- = \mu_{\text{Li}},$$

and upon substitution of expressions for the quantities $\mu_i$, the solution current density, electric potential, and salt concentration are found to be related by

$$\begin{aligned} \boldsymbol{i}_2 &= -\kappa \nabla \Phi_2 + \frac{\kappa}{F}(1 - t_+^0) \nabla \mu_{\text{salt}} \\ &= -\kappa \nabla \Phi_2 + 2RT \frac{\kappa}{F}(1 - t_+^0) \nabla \ln c, \end{aligned} \tag{A.5}$$

in agreement with the treatment in Section 81 of [17]. The solution conductivity is related to the binary diffusion coefficients:

$$\frac{1}{\kappa} = -\frac{RT}{c_{\text{T}} z_+ z_- F^2} \left(\frac{1}{D_{+-}} + \frac{c_0 t_-^0}{\nu_+ c D_{-0}}\right).$$

For the electrolyte of this study, [1,29,30]

$$\kappa = \kappa_{\max} \left(\frac{m}{m_{\max}}\right)^A \exp\left[B(m - m_{\max})^2 - A\left(\frac{m - m_{\max}}{m_{\max}}\right)\right], \tag{A.6}$$

where the molality of the salt $m$ is in units of mol/kg and is related to the molar salt concentration (mol/l) by $c = m/\rho$, and the conductivity $\kappa$ is in units of S/cm when the constants are specified as follows:

$$\left.\begin{array}{l|l} A = 0.855 & B = -0.08 \\ \kappa_{\max} = 0.00542 & m_{\max} = 0.6616 \end{array}\right| \rho = 1.204.$$

The remaining phenomenological transport relation consists of Ohm's law for relating the solid phase current density $\boldsymbol{i}_1$ and electric potential,

$$\boldsymbol{i}_1 = -\sigma \nabla \Phi_1.$$

In Appendix B, transport resistance within the carbon fibers is considered, and it is shown that for the fibers of this study, transport resistance within the fibers does not affect the current–potential relation appreciably.

### A.3. Electrochemical reaction

A Butler–Volmer equation is used to relate the local current density normal to the fiber surface $i_n$ and the potential devoted to driving the electrochemical reaction (A.1), the surface overpotential $\eta_{\text{s}}$:

$$i_n = i_0 \left[\text{e}^{(1-\beta) f \eta_{\text{s}}} - \text{e}^{-\beta f \eta_{\text{s}}}\right],$$

where $f = F/RT$ and $\beta$ is the symmetry factor. The symmetry factor is taken to be one half in this work, reflecting a strongly solvated ion [31] and consistent with measurements of the Li–$\text{Li}^+$ reaction [4,28]. The exchange current density $i_0$ is related to the anodic and cathodic rate constants, $k_{\text{a}}$ and

$k_c$, respectively, and the various reactant concentrations [17,32]:

$$i_0 = F\left[k_c c_{Li}^{+}(1-\Theta_I)\right]^{(1-\beta)}(k_a\Theta_I)^{\beta}.$$

For the conditions of this work, the surface overpotential is given by

$$\eta_s = V - U = V - \left[U^{\theta} + \frac{RT}{F}\ln\frac{1-\Theta_I}{\Theta_I} - V_{I-I}\right],$$

where $V$ is the potential of the lithiated carbon electrode relative to a lithium reference located in solution of the same liquid-phase composition, and $U$ is the open-circuit potential relative to the same reference electrode. Following the development of [4], the exchange current density is referenced to a salt concentration of 1 M and fractional occupancy of $\Theta_I = 1/2$ (i.e. $LiC_{12}$ for the graphitic carbon anode):

$$i_{0,ref} = 2i_0\big|_{c=1\,M,\Theta_I=1/2} = Fk_c^{(1-\beta)}(k_a)^{\beta}.$$

Hence, $i_{0,ref}$ is a constant and is twice the value of the exchange-current density when $\Theta_I = 1/2$ and $c = 1$ M. Recognizing that $V = \Phi_1 - \Phi_2$, one can recast the charge-transfer relation in a form better suited for numerical analysis, with the result being Eq. (A.8) (note $i_n = Fj_n$).

### A.4. Cell model

The battery is modeled as one-dimensional (see Fig. 1): the lithium electrode is at $x = 0$; the electrolyte region is $0 \le x \le \ell_1$, with the lithium reference electrode at $x = \ell_1/2$; the Li–C region is $\ell_1 \le x \le \ell_1 + \ell_2$ with the current collector at $x = \ell_1 + \ell_2$. Transport is described in each of the two regions (electrolyte and Li–C) by a system of differential equations, and the two systems are coupled together at their interface $x = \ell_1$. The dependent variables in the electrolyte region are the actual salt concentration $c$ in the pore fluid, the potential $\Phi_2$ in the pore fluid, and the volume-averaged (superficial) current density $i$. The dependent variables in the Li–C region are $c$, $\Phi_2$, and $i$, as well as $i_2$ (current density in the pore fluid), $\Phi_1$ (potential in the solid phase), and $\Theta_I$ (fractional occupancy in the solid phase).

The flux of lithium ions in the pore fluid is given by [1]

$$N_+ = -D\nabla c + \frac{t_+^0}{\epsilon_e F}i \quad \text{in the electrolyte region}$$
$$= -D\nabla c + \frac{t_+^0}{F}i_2 \quad \text{in the Li−C region}, \tag{A.7}$$

reflecting the fact that in the electrolyte region $i = \epsilon_e i_2$ (the stoichiometric coefficient $\nu_+$ has been set equal to one in the above formulae). The normal current density $i_n$ at the electrolyte–carbon interface in the Li–C region is given as $i_n = Fj_n$, where

$$Fj_n = i_{0,ref}\left(\frac{c}{c_{ref}}\right)^{1-\beta}\left[\Theta_I e^{(1-\beta)f\eta} - (1-\Theta_I)e^{-\beta f\eta}\right], \tag{A.8}$$

with

$$\eta = \Phi_1 - \Phi_2 - U^{\theta} + V_{I-I}(\Theta_I),$$

as discussed in Section A.1 and phenomenological equations.

The three field equations in the electrolyte region are:

$$\frac{\partial c}{\partial t} = D\nabla^2 c, \tag{A.9}$$

$$\frac{i}{\epsilon_e\kappa(c)} = -\nabla\Phi_2 + \frac{\nu}{f}(1-t_+^0)\nabla\ln c, \tag{A.10}$$

$$\nabla\cdot i = 0. \tag{A.11}$$

The six field equations in the Li–C region are

$$\frac{\partial c}{\partial t} = D\nabla^2 c + \frac{(1-t_+^0)}{F}\nabla\cdot i_2, \tag{A.12}$$

$$\frac{i_2}{\kappa(c)} = -\nabla\Phi_2 + \frac{\nu}{f}(1-t_+^0)\nabla\ln c, \tag{A.13}$$

$$\nabla\cdot i = 0, \tag{A.14}$$

$$\frac{\epsilon_2}{F}\nabla\cdot i_2 = -\epsilon_1 c_s\frac{\partial\Theta_I}{\partial t}, \tag{A.15}$$

$$i - \epsilon_2 i_2 = -\epsilon_1\sigma\nabla\Phi_1, \tag{A.16}$$

$$\epsilon_1 c_s\frac{\partial\Theta_I}{\partial t} = -a_s j_n. \tag{A.17}$$

The pore-fluid quantities ($c$, $i_2$, $\Phi_2$) are local averages over the liquid phase and are thus defined at all positions $x$. Similarly the solid-phase variables $\Phi_1$ and $\Theta_I$ are local averages over the solid phase and are defined everywhere in the Li–C region as well. The normal fluxes $j_n$ at the fiber surfaces appear also as local averages in Eq. (A.17) (see also Appendix B). Eqs. (A.9) and (A.12) express material balance for the salt [1]. Eqs. (A.10) and (A.13) express an Ohm's law relation for the solution phase (cf. Eq. (A.5)). Note that the stoichiometric coefficient $\nu = \nu_+ + \nu_-$ is 2 for the 1:1 electrolyte of this study. Eqs. (A.11) and (A.14) express conservation of charge. Eq. (A.15) expresses charge conservation in the liquid phase. Eq. (A.16) is an Ohm's law relation for current density in the solid phase. Eq. (A.17) is the dimensioned form of Eq. (B.7) derived in Appendix B and results from a material balance on the guest species within the insertion electrode.

Boundary conditions for the two regions are:

$$\epsilon_e F N_+ = i \text{ at } x = 0, \tag{A.18}$$

$$\Phi_2 = 0 \text{ at } x = \frac{\ell_1}{2}, \tag{A.19}$$

Table 2
Dimensionless form of the model equations

| Li electrode, $X = 0$ | Electrolyte | Interface, $X = 1$ | Li–C electrode | Current collector, $X = L$ |
|---|---|---|---|---|
| $\tilde{i} = -\epsilon_e C'/(1 - t_+^0)$ | $\partial C/\partial\tau = C''$ | $(\epsilon_e C')_{\text{left}} = (\epsilon_2 C')_{\text{right}}$ | $\partial C/\partial\tau = C'' + (1 - t_+^0)(\tilde{i}_2)'$ | $C' = 0$ |
| $\tilde{i}/[\epsilon_e\tilde{\kappa}(C)] = -\Psi'_2 +$ | $\tilde{i}/[\epsilon_e\tilde{\kappa}(C)] = -\Psi'_2 +$ | $\tilde{i}/[\epsilon_e\tilde{\kappa}(C)] = [-\Psi'_2 +$ | $\tilde{i}_2/\tilde{\kappa}(C) = -\Psi'_2 +$ | $\tilde{i}_2/\tilde{\kappa}(C) = -\Psi'_2 +$ |
| $\nu(1 - t_+^0)(\ln C)'$ | $\nu(1 - t_+^0)(\ln C)'$ or $\Psi_2 = 0$ when $X = 1/2$ | $\nu(1 - t_+^0)(\ln C)']_{\text{left}}$ | $\nu(1 - t_+^0)(\ln C)'$ | $\nu(1 - t_+^0)(\ln C)'$ |
| $(\tilde{i})' = 0$ | $(\tilde{i})' = 0$ | $\epsilon_2\tilde{i}_2 = \tilde{i}$ | $(\tilde{i})' = 0$ | $(\tilde{i})' = 0$ |
| – | – | $\epsilon_2(\tilde{i}_2)'_{\text{right}} = -\epsilon_1 C_s \partial\Theta_1/\partial\tau$ | $\epsilon_2(\tilde{i}_2)' = -\epsilon_1 C_s \partial\Theta_1/\partial\tau$ | $\tilde{i}_2 = 0$ |
| – | – | $\tilde{i} - \epsilon_2\tilde{i}_2 = -\epsilon_1\tilde{\sigma}(\Psi'_1)_{\text{right}}$ | $\tilde{i} - \epsilon_2\tilde{i}_2 = -\epsilon_1\tilde{\sigma}\Psi'_1$ | $\tilde{i} = \tilde{i}_{\text{cell}}$ or $\Psi_1 = fV$ |
| – | – | $\epsilon_1 C_s \partial\Theta_1/\partial\tau = -\delta J_n$ | $\epsilon_1 C_s \partial\Theta_1/\partial\tau = -\delta J_n$ | $\epsilon_1 C_s \partial\Theta_1/\partial\tau = -\delta J_n$ |

$J_n = (C/C_{\text{ref}})^{1-\beta}[\Theta_1 e^{(1-\beta)\tilde{\eta}} - (1 - \Theta_1)e^{-\beta\tilde{\eta}}]$, $\tilde{\eta} = \Psi_1 - \Psi_2 - fU^\theta + fV_{1-1}(\Theta_1)$. $\partial/\partial X$ is represented with a prime. Table 3 gives the definitions of the dimensionless quantities. Note that a constant transference number has been assumed, consistent with available literature data. For the simulations of this work, $\Theta_1(0, X) = 0.02$, $C(0, X) = 1.3$, and results are presented for the fourth cycle (cf. Fig. 6).

$$\left.\begin{aligned} &\lim_{x\to\ell_1^-}\epsilon_e\frac{\partial c}{\partial x} = \lim_{x\to\ell_1^+}\epsilon_2\frac{\partial c}{\partial x}\\ &\lim_{x\to\ell_1^-} c = \lim_{x\to\ell_1^+} c\\ &\lim_{x\to\ell_1^-} i = \lim_{x\to\ell_1^+} i\\ &\lim_{x\to\ell_1^-}\Phi_2 = \lim_{x\to\ell_1^+}\Phi_2\\ &\lim_{x\to\ell_1^+} i - \epsilon_2 i_2 = 0 \end{aligned}\right\} \text{at } x = \ell_1, \tag{A.20}$$

$$\left.\begin{aligned} &N_+ = 0\\ &i_2 = 0\\ &\Phi_1 = V \quad \text{or} \quad i = i_{\text{cell}} \end{aligned}\right\} \text{at } x = \ell_1 + \ell_2. \tag{A.21}$$

The boundary condition at $x = 0$ states that current is carried by the lithium ion at the lithium electrode. The boundary condition at $x = \ell_1/2$ sets the reference electrode at this point. The boundary conditions at $x = \ell_1$ specify continuity of various physical quantities at the interface, as well as the fact that the solid-phase current is zero at the interface. Both the salt flux and current vanish at the current collector, as stated in the first two conditions at $x = \ell_1 + \ell_2$. The two possibilities for the last condition are for either voltage or current control.

Table 2 restates these equations in dimensionless form and gives an indication of how they can be discretized for numerical solution. The boundary conditions expressing continuity of the dependent variables at $x = \ell_1$ are automatically implemented in the finite difference scheme, because these variables must be single-valued at each node; thus these conditions do not appear in the table. Note in particular that the continuity of $\Psi_2$ at the interface serves as a boundary condition for the second field equation in the Li–C region.

## Appendix B

Our purpose in this appendix is to show that the model equations proposed in [1], which include diffusional resistance within the solid phase, can be simplified when a dimensionless group ($\zeta$, defined below) that characterizes the time of transition to steady-state for diffusion within the insertion electrode is small. At the end of appendix, we show how these simplified equations can also apply under somewhat more general assumptions than those utilized in [1].

The material-balance equation for lithium in the carbon phase is:

$$\frac{\partial\Theta_I}{\partial t} = D_I\nabla\cdot\left[\left(1 + \frac{d\ln\gamma_I}{d\ln\Theta_I}\right)\nabla\Theta_I\right].$$

The thermodynamic quantity $(1 + d\ln\gamma_I/d\ln\Theta_I)$, which can be evaluated from open-circuit potential data such as that shown in Fig. 4, has been shown to be a strong function of guest occupancy [4]. At the fiber surface, a Butler–Volmer condition is employed [1]:

$$-D_I c_s\left(1 + \frac{d\ln\gamma_I}{d\ln\Theta_I}\right)\nabla\Theta_I\cdot\boldsymbol{n} = j_n(c, \Phi_1, \Phi_2, \Theta_I),$$

where the definition of $j_n$ is given by Eq. (A.8), and $\boldsymbol{n}$ is an outward unit normal on the fiber surface. An initial condition of the form

$$\Theta_I(t = 0) = \Theta_I^0,$$

is also assumed. The problem can be put in dimensionless form using the following definitions:

$$\alpha = \frac{a i_{0,\text{ref}}}{F D_I c_s} \quad \zeta = \frac{D}{D_I}\left(\frac{a}{\ell_1}\right)^2 \quad \bar{\nabla} = a\nabla,$$

in addition to the dimensionless groups given in Table 3, where $a$ is a characteristic length for the fiber; e.g. the fiber

Table 3
Dimensionless quantities

| | | |
|---|---|---|
| $\tau = tD/\ell_1^2$ | $X = x/\ell_1$ | $L = (\ell_1 + \ell_2)/\ell_1$ |
| $C = c/c^0$ | $C_{\text{ref}} = c_{\text{ref}}/c^0$ | $C_s = c_s/c^0$ |
| $\tilde{N}_+ = \ell_1 N_+/(c^0 D)$ | $\tilde{i} = \ell_1 i/(F c^0 D)$ | $\tilde{i}_2 = \ell_1 i_2/(F c^0 D)$ |
| $\Psi_1 = f\Phi_1$ | $\Psi_2 = f\Phi_2$ | $\tilde{\eta} = f\eta$ |
| $\tilde{\kappa}(C) = F^2\kappa(c)/(F c^0 D)$ | $\tilde{\sigma} = F^2\sigma/(F c^0 D)$ | $\delta = a_s\ell_1^2 i_{0,\text{ref}}/(c^0 D F)$ |

Along with the dimensionless dependent and independent variables are given the dimensionless parameters $\delta$ and $L$, which can be altered to optimize battery performance.

radius for cylindrical or spherical fiber; for this study, $a \approx 2 \times 10^{-6}$ cm. The scaled forms of the above equations are:

$$\zeta \frac{\partial \Theta_I}{\partial \tau} = \bar{\nabla} \cdot \left[ \left( 1 + \frac{d \ln \gamma_I}{d \ln \Theta_I} \right) \bar{\nabla} \Theta_I \right], \tag{B.1}$$

$$-\left( 1 + \frac{d \ln \gamma_I}{d \ln \Theta_I} \right) \bar{\nabla} \Theta_I \cdot \boldsymbol{n} = \alpha J_n(C, \Psi_1, \Psi_2, \Theta_I). \tag{B.2}$$

For practical insertion-electrode materials and particle sizes, $\zeta$ is usually less than 0.001. Define $\Theta_{I_0}$ to be the solution to the above equations in the limit as $\zeta \to 0$. $\Theta_{I_0}$ will be an accurate approximation to the solutions of Eqs. (B.1) and (B.2) when $\zeta$ is small.

Before proceeding, it is useful to note the parameter relationship

$$\frac{\delta \zeta}{\alpha} = a_s a C_s. \tag{B.3}$$

In the following analysis, it will be assumed that $\delta$, $\zeta$, $a_s a$, and $C_s$ are constants whose values can be chosen independently. A value for $\alpha$ is then determined by Eq. (B.3) in terms of these other dimensionless groups.

To determine $\Theta_{I_0}$ one must solve

$$0 = \bar{\nabla} \cdot \left[ \left( 1 + \left. \frac{d \ln \gamma_I}{d \ln \Theta_I} \right|_{\Theta_{I_0}} \right) \bar{\nabla} \Theta_{I_0} \right], \tag{B.4}$$

$$-\left( 1 + \left. \frac{d \ln \gamma_I}{d \ln \Theta_I} \right|_{\Theta_{I_0}} \right) \bar{\nabla} \Theta_{I_0} \cdot \boldsymbol{n} = \alpha J_n(C, \Psi_1, \Psi_2, \Theta_{I_0}). \tag{B.5}$$

If one can choose a constant value of $\Theta_{I_0}$ such that $\alpha J_n(C, \Psi_1, \Psi_2, \Theta_{I_0}) = 0$ at all boundary points of the fiber, then this constant value is also a solution to Eqs. (B.4) and (B.5). Eq. (B.3) guarantees this, because it implies that $\alpha$ tends to zero in the limit as $\zeta \to 0$.

To proceed further we recall that in the treatments provided in [1], the variables $c$, $\Phi$, and $\Phi_2$ are assumed constant over the surface of the carbon fiber; we shall make the same assumption. By integrating Eq. (B.1) over the fiber, one then finds that

$$\text{Volume}\, \zeta \frac{\partial \Theta_{I_0}}{\partial \tau} = -\text{Area}\, \alpha J_n(C, \Psi_1, \Psi_2, \Theta_{I_0}), \tag{B.6}$$

in the limit as $\zeta \to 0$, where the volume and area of the fiber must be computed using dimensionless coordinates in which the characteristic fiber size is order one, so that on average

$$\frac{\text{Area}}{\text{Volume}} = \frac{a_s a}{\epsilon_1}.$$

Using Eq. (B.3), one can rewrite Eq. (B.6) as

$$\epsilon_1 C_s \frac{\partial \Theta_{I_0}}{\partial \tau} = -\delta J_n(C, \Psi_1, \Psi_2, \Theta_{I_0}). \tag{B.7}$$

Thus, the time evolution of $\Theta_{I_0}$ is determined by the initial state $\Theta_I^0$ and Eq. (B.7). Consistent with this development, in [6] Eq. (B.7) was employed instead of solving a transient diffusion equation (e.g. Eq. (B.1)) for the intercalate species (analysis of two-dimensional effects in thin-film lithium-ion batteries was focused in [6]).

The parameter $\delta$ measures how facile the kinetics of the electrochemical reaction (A.1) is, as can be seen from Eq. (B.7); letting $\delta$ tend to infinity forces the equilibrium condition $J_n(C, \Psi_1, \Psi_2, \Theta_{I_0}) = 0$.

One can estimate the error in the approximate solution $\Theta_{I_0}$ by considering the residual in Eqs. (B.1) and (B.3) when $\Theta_I = \Theta_{I_0}$. Eq. (B.7) can then be used to determine time derivatives of $\Theta_{I_0}$. If these time derivatives are too large, then Eq. (B.4) becomes a poor approximation to Eq. (B.1), and $\Theta_{I_0}$ is a poor approximation to $\Theta_I$. Thus, $\Theta_{I_0}$ can be viewed as a good approximation as long as $\zeta \partial \Theta_{I_0} / \partial \tau$ remains small. Using Eq. (B.7), one sees that this is equivalent to the condition

$$\frac{\delta \zeta}{\epsilon_1 C_s} |J_n(C, \Psi_1, \Psi_2, \Theta_{I_0})| \ll 1.$$

Similarly, to show that $\Theta_{I_0}$ comes close to satisfying Eq. (B.2) the condition

$$\alpha |J_n(C, \Psi_1, \Psi_2, \Theta_{I_0})| = \frac{\delta \zeta}{a_s a C_s} |J_n(C, \Psi_1, \Psi_2, \Theta_{I_0})| \ll 1$$

must also hold.

Although the approach outlined here is valid only when $\zeta \ll 1$, it shows that the model equations will not change (in the limit of small $\zeta$) even if the activity coefficients appearing in the flux expression for lithium in carbon fibers are nonzero. This is significant, because these coefficients can vary over a full order of magnitude [4]. In addition, all that is required with regard to the insertion particle shape is to assume that its geometry is simple enough so that its characteristic dimensions are all of the same order (e.g. maximum and minimum particle dimensions).

It should also be mentioned that the analysis we have given and those of [1] depend on the assumption that the variables $C$, $\Psi_1$, and $\Psi_2$ are constant on the scale of the fibers. This assumption is only approximately true, and it conceivably gives rise to errors (in both models) that are as large or larger than the errors arising from the approximation $\Theta_I \approx \Theta_{I_0}$. Clearly a more detailed derivation of the governing equations for a porous electrode would be necessary in order to quantify these issues.

## References

[1] M. Doyle, T.F. Fuller, J. Newman, J. Electrochem. Soc. 140 (1993) 1526;
T.F. Fuller, M. Doyle, J. Newman, J. Electrochem. Soc. 141 (1994) 1;
T.F. Fuller, M. Doyle, J. Newman, J. Electrochem. Soc. 141 (1994) 982;
M. Doyle, J. Newman, J. Reimers, J. Power Sources 52 (1994) 211;
M. Doyle, J. Newman, A.S. Gozdz, C.N. Schmutz, J.-M. Tarascon, J. Electrochem. Soc. 143 (1996) 1890;

R. Darling, J. Newman, J. Electrochem. Soc. 144 (1997) 4201;
J.P. Meyers, M. Doyle, R.M. Darling, J. Newman, J. Electrochem. Soc. 147 (2000) 2930. .
[2] T. Uchida, Y. Morikawa, H. Ikuta, M. Wakihara, K. Suzuki, J. Electrochem. Soc. 143 (1996) 2606.
[3] M.W. Verbrugge, B.J. Koch, J. Electrochem. Soc. 143 (1996) 24.
[4] M.W. Verbrugge, B.J. Koch, J. Electrochem. Soc. 143 (1996) 600.
[5] M.W. Verbrugge, B.J. Koch, J. Electrochem. Soc. 146 (1999) 833.
[6] D.R. Baker, M.W. Verbrugge, J. Electrochem. Soc. 146 (1999) 2413.
[7] P. Arora, M. Doyle, R.E. White, J. Electrochem. Soc. 146 (1999) 3543.
[8] J.I. Yamaki, M. Egashira, S. Okada, J. Electrochem. Soc. 147 (2000) 460.
[9] G.G. Botte, R.E. White, J. Electrochem. Soc. 148 (2001) A54.
[10] G.G. Tibbetts, SAE 901036, 1990.
[11] G.G. Tibbetts, D.W. Gorkiewicz, R.L. Alig, Carbon 31 (1993) 809.
[12] G.G. Tibbetts, G.L. Doll, D.W. Gorkiewicz, J.J. Moleski, T.A. Perry, C.J. Dasch, M.J. Balogh, Carbon 31 (1993) 1039.
[13] K. West, T. Jacobsen, S. Atlung, J. Electrochem. Soc. 129 (1982) 1480.
[14] M. Viitanen, J. Electrochem. Soc. 140 (1993) 936.
[15] Q.M. Yang, M. Ciureanu, D.H. Ryan, J.O. Ström-Olsen, J. Electrochem. Soc. 141 (1994) 2108;
Q.M. Yang, M. Ciureanu, D.H. Ryan, J.O. Ström-Olsen, J. Electrochem. Soc. 141 (1994) 2113.
[16] P. De Vidts, J. Delgado, R.E. White, J. Electrochem. Soc. 142 (1995) 4006.
[17] J. Newman, Electrochemical Systems, Prentice-Hall, Englewood Cliffs, NJ, 1973.
[18] A.J. Bard, L.R. Faulkner, Electrochemical Methods, Wiley, New York, 1980.
[19] M. Doyle, T.F. Fuller, J. Newman, J. Electrochem. Soc. 140 (1993) 1526.
[20] T.R. Jow, C.C. Liang, J. Electrochem. Soc. 129 (1982) 1429.
[21] M.W. Verbrugge, H. Gu, A chapter in PV 94-22, topics in electrochemical engineering, in: J. Newman, R.E. White (Eds.), Proceedings of the Douglas N. Bennion Memorial Symposium, The Electrochemical Society, 1994.
[22] R. Fong, U. von Sacken, J.R. Dahn, J. Electrochem. Soc. 137 (1990) 2009.
[23] E.A. Guggenheim, Thermodynamics, 6th Edition, North-Holland, Amsterdam, 1977.
[24] K. Wohl, Trans. AIChE 42 (1946) 215.
[25] L. Onsager, Ann. N.Y. Acad. Sci. 46 (1945) 241.
[26] J.O. Hirschfelder, C.F. Curtiss, R.B. Bird, Molecular Theory of Gases and Liquids, Wiley, New York, p. 718, 1954.
[27] R.B. Bird, W.E. Stewart, E.N. Lightfoot, Transport Phenomena, Wiley, New York, p. 568, 1960.
[28] M.W. Verbrugge, B.J. Koch, J. Electrochem. Soc. 141 (1994) 3053.
[29] J. Barthel, H.-J. Gores, G. Schmeer, Ber. Bunsenges. Phys. Chem. 83 (1979) 911.
[30] H.-J. Gores, J. Barthel, J. Solution Chem. 9 (1980) 939.
[31] V.G. Levich, Present state of the theory of oxidation–reduction in solution (bulk and electrode reaction), a chapter, in: P. Delahay, C.W. Tobias (Eds.), Advances in Electrochemistry and Electrochemical Engineering, Vol. 4, Wiley/Interscience, New York, 1966.
[32] K.J. Vetter, in: S. Bruckenstein, B. Howard (Eds.), Elektrochemische Kinetik, Springer, Berlin, 1961 (Electrochemical Kinetics, Academic Press, New York, 1967).
[33] D. Aurbach, Y. Ein-Eli, O. Chusid (Youngman), Y. Carmeli, M. Babai, H. Yamin, J. Electrochem. Soc. 141 (1994) 603.
[34] J.O. Besenhard, M. Winter, J. Yang, W. Biberacher, J. Power. Sources 54 (1995) 228.
[35] D. Aurbach, Y. Ein-Eli, J. Electrochem. Soc. 142 (1995) 1746.
[36] J.S. Gnanaraj, M.D. Levi, E. Levi, G. Salitra, D. Aurbach, J.E. Fishcher, A. Claye, J. Electrochem. Soc. 148 (2001) A525.
[37] G. Eichinger, J. Electroanal. Chem. 74 (1976) 183.
[38] M. Arakawa, J. Yamaki, J. Electroanal. Chem. 219 (1987) 273.
[39] R. Jasinski, Electrochemistry and Application of Propylene Carbonate, a chapter, in: P. Delahay, C.W. Tobias (Eds.), Advances in Electrochemistry and Electrochemical Engineering, Vol. 8, Wiley/Interscience, New York, 1971.